

Laboratory Studies of Wave-Current Interaction: Kinematics of the Strong Interaction

RONALD J. LAI

David Taylor Research Center, Bethesda, Maryland

STEVEN R. LONG

NASA Goddard Space Flight Center, Wallops Flight Facility, Wallops Island, Virginia

NORDEN E. HUANG¹

Office of Naval Research, Arlington, Virginia

Controlled laboratory experiments have been conducted to study the kinematics of wave-current interactions. The results confirm the conservation of waves under the steady state condition. The data also show that the kinematic effect of the current on waves can be treated as a simple Doppler shift. After the Doppler correction, the kinematics of the waves (either breaking or nonbreaking) follows the linear theory very well. The experiments also confirm the blockage of the waves by currents when the ratio \bar{u}/C_0 approaches $-1/4$.

1. INTRODUCTION

Wave-current interactions encompass a variety of complicated phenomena; few of them have been thoroughly studied. There are actually two seemingly unrelated types of interactions between waves and currents: the strong interactions and the weak ones. The strong interactions concern the changes of the waves by the currents detectable within one wave period or one wave length. For these effects to show, however, the current strength has to be comparable to that of the wave group (or phase) velocity, and it also has to show substantial variations during the life span of the waves. The theoretical foundation for describing the strong interactions is well established (see, for example, *Phillips* [1977]); the approach is to apply various conservation laws to the mean properties of linear waves. The most recent results are summarized by *Peregrine* [1976], and *Peregrine and Jonsson* [1983]. As was pointed out in the review by *Peregrine* [1976], almost all of these results are either analytic or numerical; few quantitative observations are available to confirm or to dispute them. The reason for the lack of such observations is the requirement of simultaneous measurements of the current and the wave fields in both wave number and frequency spaces. The wave number data need spatial coverage of the wave field, which is hard to make.

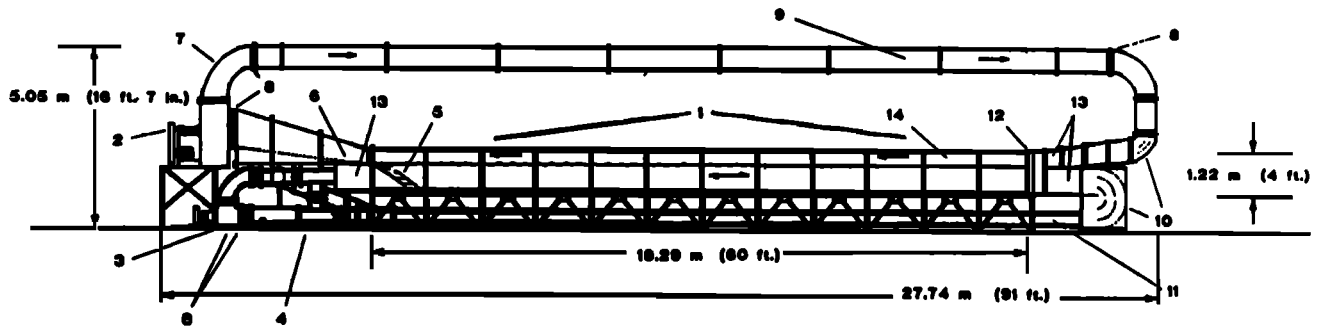
The weak interactions, on the other hand, concern the changes of the waves by the currents detectable only through long-term evolution of the waves. For the weak interaction effects to show, the current strength can be as low as $(ak)^3$ times the phase velocity, as was shown by *Mollo-Christensen* [1982]. Recently, more specific analyses

are reported by *Gerber* [1987]. Qualitative observations by *Bliven et al.* [1986] suggest that the weak interactions could be responsible for the suppression of the Benjamin-Feir instability in the laboratory. Since the effects are so subtle, they are seldom observed in the field. However, these results represent only the beginning of serious investigations on the latter type of interactions.

Since the conditions for the weak and the strong wave-current interactions are so different, the phenomena should be expected to occur under different environments. The low current strength requirement makes the weak interactions the more prevailing of the two, but also the more subtle. The cumulated effects of the weak yet persistent wave-current interactions, however, can alter the wave field similar to the weakly nonlinear wave-wave interactions [*Yuen and Lake*, 1982]. Laboratory as well as field confirmations for all the weak interactions, whether wave-wave or wave-current under more realistic environmental conditions, are the elusive targets for wave investigators. The high current strength requirement, on the other hand, makes the strong interactions observable only at special locations such as at harbor entrances, river mouths [*Gonzalez*, 1984], oceanic fronts [*McClain et al.*, 1982], and along the major oceanic current systems or over the eddies [*Mallory*, 1974; *Mapp et al.*, 1985]. Yet the strong wave-current interactions can also be a common phenomena, if one counts the long-short wave-wave interactions as a special case where the orbital velocity of the long wave can be treated as a periodic current field for the short waves [*Phillips*, 1977; *Longuet-Higgins*, 1987].

Important as the wave-current interactions are in determining the final sea state, our knowledge is quite incomplete. Even for the strong interactions, we still need the observational confirmations and validations. In the present paper we will present our first set of experimental results concerning the kinematics of the strong wave-current interactions only, beginning with the experimental conditions and procedures

¹Permanently at NASA Goddard Space Flight Center, Greenbelt, Maryland.



- | | |
|---------------------------------|---------------------------|
| 1. Test Section | 8. Flexible Joint |
| 2. Trane 38AFSW Fan | 9. Air Flow Duct |
| 3. Ingersoll-Rand 6000 GPM Pump | 10. Flow Turning Vanes |
| 4. Valve Assembly | 11. Fiberglass Piping |
| 5. Primary Beach | 12. Random Wave Generator |
| 6. Secondary Beach | 13. Honeycomb Section |
| 7. Fan Discharge | 14. Plate Glass Side |

Fig. 1. The wind, wave, and current interaction research facility at NASA Wallops Flight Facility. Numbered parts are as follows: (1) test section, (2) suction fan, (3) 6000 gal./min water pump, (4) pump valve assembly, (5) primary beach, (6) secondary beach, (7) fan discharge, (8) flexible joint, (9) air-flow duct, (10) flow turning vanes, (11) fiberglass piping, (12) programmable wave generator, (13) air and water flow rectifying honeycomb sections, (14) plate glass side.

and followed by the data analysis methods, the salient results, and the discussion and conclusions.

2. EXPERIMENTAL CONDITIONS AND PROCEDURES

The experiments are conducted in the Wind-Wave-Current Interaction Research Facility at NASA Wallops Flight Facility, Wallops Island, Virginia. The tank, as shown in Figure 1, has a test section with dimensions of 1.22-m depth, 0.91-m width, and 18.3-m length with an operational water depth of 0.76 m, as described by *Huang and Long* [1980]. The operational water depth allows 0.46 m in the vertical for the wind, which is generated by a suction fan located at the left end of the tank that gives the wind its direction from the right to left only, when viewed as in

Figure 1. For this series of experiments, the wind was not used at all. Currents from 0 up to 0.5 m/s can be generated in the tank by a pump also located at the left end of the tank. A pipe system allows the water to flow in either direction in the tank. For this set of experiments, only the right-to-left direction is used because of the better surge tank at the right end that gives smoother currents. To aid in smoothing the water flow, a plastic honeycomb section 0.30 m in length and tube of 0.01 m was placed in the entire tank cross section as the water exited the sump. In order to create a current field with spatially variable speed, a false bottom was installed in the tank at the middle part of the test section, which consists of a flat top 0.30 m in height and 2.44 m in length, with two symmetric ramps extending 1.22 m on each side as shown schematically in Figure 2. With the false bottom, the water depth is reduced to a minimum of 0.45 m.

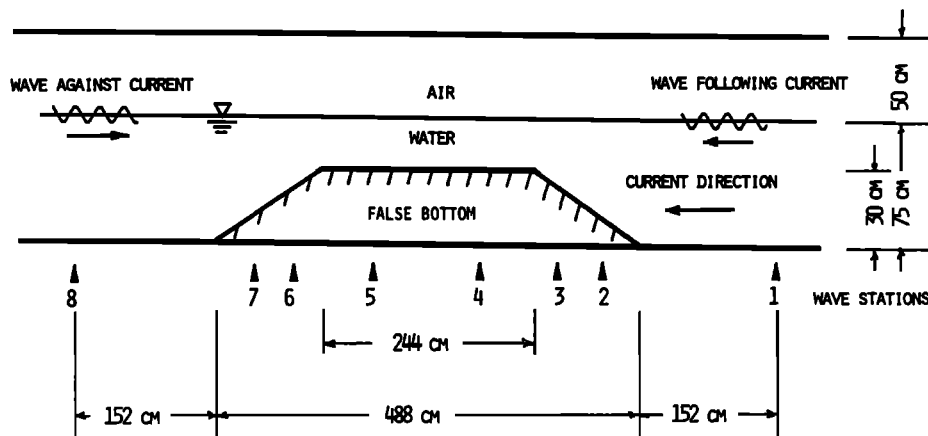


Fig. 2. Schematic of the wave probe stations relative to the false bottom.

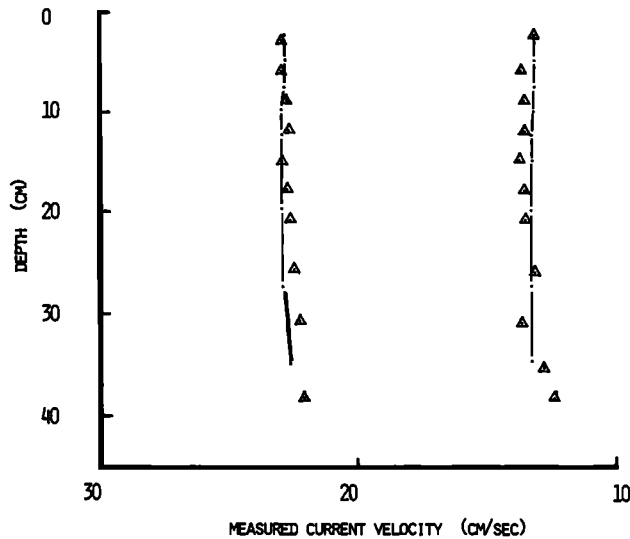


Fig. 3. Comparisons of the current values measured at station 5 by the TSI laser Doppler velocimeter (dashed-dotted lines) and the Marsh-McBirney electromagnetic current meter (triangles).

Waves can be generated both by the wind and by two programmable wave makers located at either end of the tank. In order not to impede the current flow, the active part of the wave maker consists of a hydraulically driven paddle which extends across the tank, but is only 10 cm in height, with the mean water line at the middle of the driving plate. The front face of the paddle is flat, but the back is streamlined to enable the current to pass with minimum disturbance. For this set of experiments, monochromatic waves of four different frequencies (2.25, 2.0, 1.75, and 1.5 Hz) were used with two different amplitudes for each frequency.

Both a TSI laser Doppler velocimeter (LDV) model 9100-7 two-color four-beam system, and a Marsh-McBirney electromagnetic (EM) current meter (model 523) were used to measure the currents. The differences between the two methods in the temporal mean current observed were typically within 5% for each individual reading as shown in Figure 3. Most of the current measurements, however, are

made with the Marsh-McBirney, for it can be easily deployed at various positions coincident with the wave stations. The LDV system is deployed at station 5 as a reference only.

Since the LDV system has a fast time response, and since it also has a mean frequency offset, it can measure the reversal of the current at a high rate to reveal the turbulent characteristics. Some typical data are examined more carefully as follows. Figures 4a and 4b show the probability density functions of the current at the depths 5 and 27.5 cm under a low mean current condition. The influence of the wave orbital velocity is clearly visible at the shallow depth of 5 cm, as shown by the bimodal distribution of the velocity. Such an influence is no longer visible at the depth of 27.5 cm. Although the mean velocity values at the two different depths are similar (7.91 cm/s at 5-cm depth and 8.05 cm/s at 27.5-cm depth), the variances change substantially (1.32 cm/s at 5-cm depth and 0.33 cm/s at 27.5-cm depth.) Figures 5a and 5b show the corresponding probability density functions for a higher mean current condition. For this case, the influence of the orbital velocity reversal is no longer visible. The mean current values at both depths are again very close (23.04 for 5-cm depth and 23.32 cm/s for 27.5-cm depth), and the variances are again different (2.04 cm/s for 5-cm depth and 0.78 cm/s for the 27.5-cm depth.) For all the cases checked, the identical trend repeats for the vertical components as well. It is, however, puzzling to find that the velocity measured at the shallower depth cannot be treated as a simple superposition of the orbital velocity and the mean current; the variance is consistently lower than the rms orbital velocity computed according to the amplitude and frequency observed. We cannot offer any further explanation for this anomaly.

The turbulence intensity of the current away from the water surface is generally in the 3% to 4% range, which is low for water flow; therefore for the subsequent analysis the mean current is a meaningful representation of the current condition.

Capacitance probes were used for wave elevation measurements. These probes have a accuracy of better than 5% as reported by *Huang and Long [1980]*. A total of 16 wave

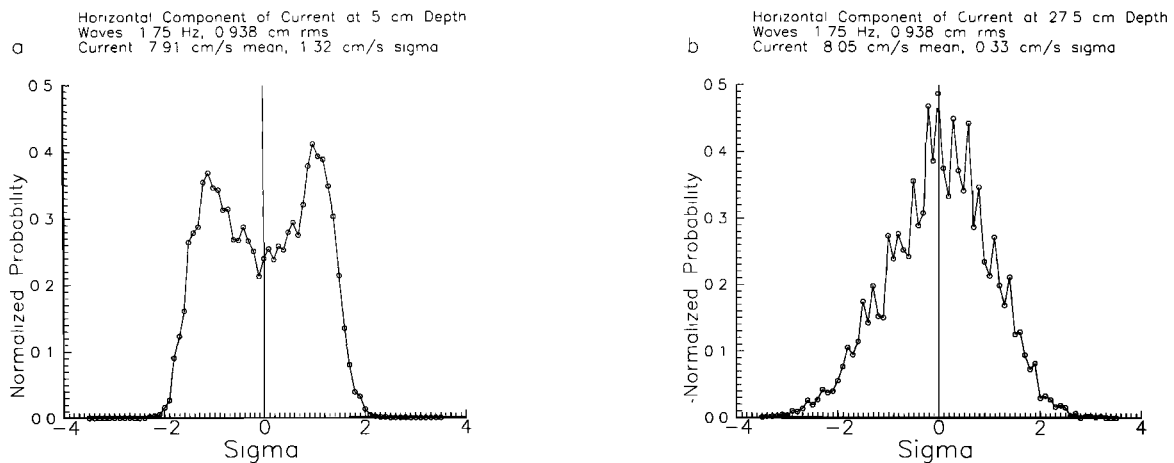


Fig. 4. Typical probability density functions for the horizontal component current under a wave (rms elevation 0.938 cm; 1.75 Hz) propagating against a low current measured with the LDV system at two different depths: (a) 5-cm depth (mean current, 7.91 cm/s; variance, 1.32 cm/s) and (b) 27.5-cm depth (mean current, 8.05 cm/s; variance, 0.33 cm/s).

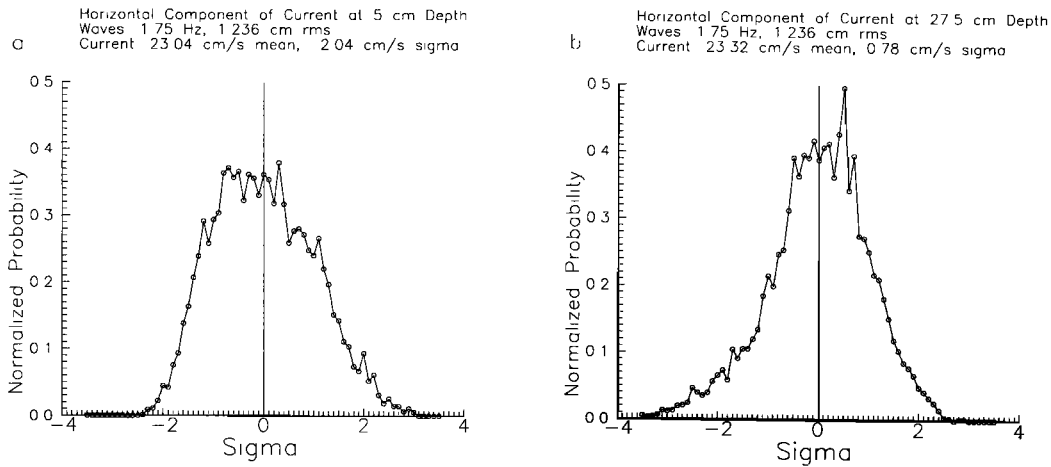


Fig. 5. Typical probability density functions for the horizontal component current under a wave (rms elevation 1.236 cm; 1.75 Hz) propagating against a high current measured with the LDV system at two different depths: (a) 5-cm depth (mean current, 23.04 cm/s; variance, 2.04 cm/s) and (b) 27.7-cm depth (mean current, 23.32 cm/s; variance, 0.78 cm/s).

probes were used at eight stations as indicated in Figure 2. At each station, two probes are deployed at a fixed spacing of 0.01 m to measure both wave elevations and slopes through differencing.

The experiment started with a preselected current setting. The pump was operated at the same setting for the whole series of different wave conditions before the current condition was changed. At the beginning of each run, waves of a preselected frequency and amplitude were generated by the programmable wave maker at either end of the tank so that the different conditions of waves with and opposing the currents could be created. At least 10 min were allowed to lapse for the test condition to settle down to a steady state before data collection began. All the data were digitized and processed by two HP1000 computers. The detailed analyses steps and the results are given in the following section.

3. DATA ANALYSES AND RESULTS

Data analyses and the results of currents and waves are presented as follows.

3.1. Current

At each wave measurement station, a current profile consisting of at least ten 1.5-min mean readings at various depths was made with the Marsh-McBirney current meter. Typical current profiles without waves are shown in Figure 6. Because there was little detectable shear above the 0.40-m depth where the waves could sense the differences and because the turbulence intensity in the current was low as was discussed in the last section, the measured current was defined simply as the depth-averaged value \bar{u} , computed by:

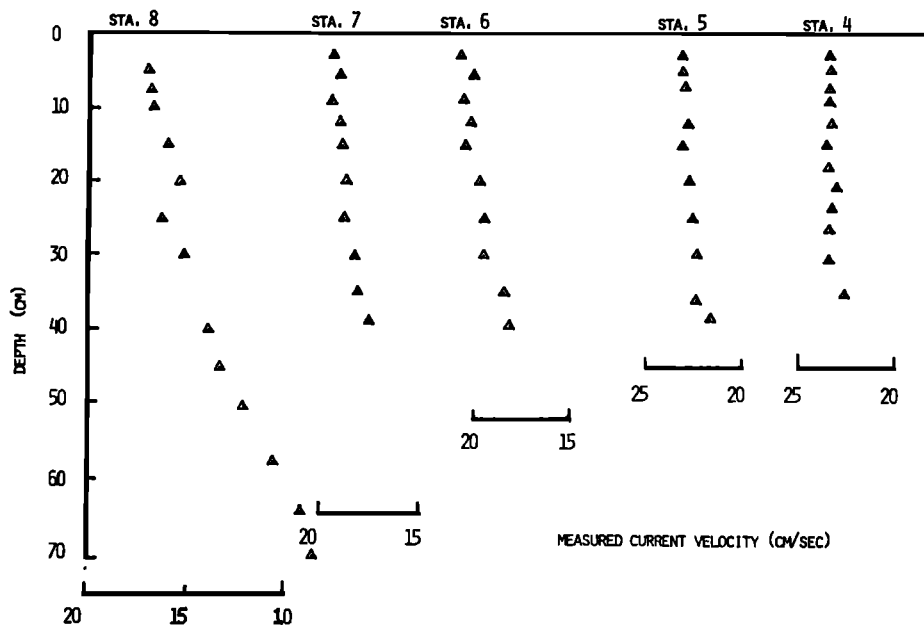


Fig. 6. Typical current profiles measured with the Marsh-McBirney electromagnetic current meter.

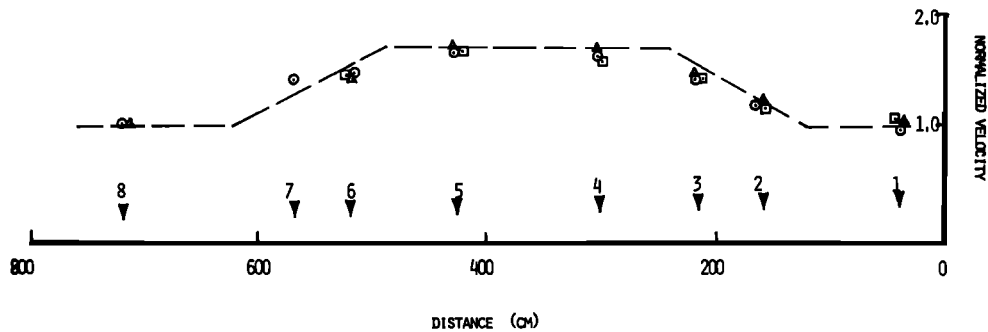


Fig. 7. Variations of the normalized mean current along the test section over the false bottom. Current at station 1 is taken as the base in the normalization. Symbols are squares, $U = 13.0$ cm/s; triangles, $u = 8.30$ cm/s; and circles, $u = 5.31$ cm/s.

$$\bar{u} = \frac{1}{z_2 - z_1} \int_{z_1}^{z_2} u(z) dz \quad (1)$$

in which $u(z)$ is the individual reading at the vertical coordinate z , and z_1 and z_2 are the top and bottom depths of the measurements. The mean current values, normalized with respect to the station 1 reading, reflects the change of the cross section areas very well, as is shown in Figure 7. These profiling measurements were repeated for each test run. While the Marsh-McBirney current meter was used to make the current profile measurements, the LDV was also profiling at station 5, with a 3-min averaged value at each level to provide a reference.

The influence of waves on the mean current profiles appeared to be small. Typical comparisons of the currents with and without the waves are shown in Figures 8a and 8b for the stations number 5 and 8. At station 5 over the top of the false bottom, there was no detectable difference in the current data with or without waves for all currents. At station 8, however, a slight difference could be seen, especially for the readings near the surface with waves propagating against the currents. The differences observed were that the cases with waves always gave a slightly lower current value. Since the nonbreaking waves can induce current only in the Lagrangian frame, it should not appear in the Eulerian fixed point measurements. One possibility is due to the strong reverse flow associated with the orbital particle motion. Whether the EM current meter can or cannot successfully monitor strong fluctuations with reverse flow is quite controversial (see, for example, *Aubrey and Trowbridge* [1985] and *Guza* [1988]). Because such variation was absent in the LDV data, the simplest explanation is that the difference is within the EM current meter instrument precision limit. Furthermore, if depth-averaged current values are computed according to equation (1), the difference between the cases with and without waves for the EM current meter is within 6%, which is comparable to the difference between the LDV and the EM current meter as discussed in the previous section. Thus the explanation based on the precision limit seems to be reasonable.

3.2. Non-Breaking Waves

As was stated in the preceding section, the wave data were collected at each station by two capacitance probes, from

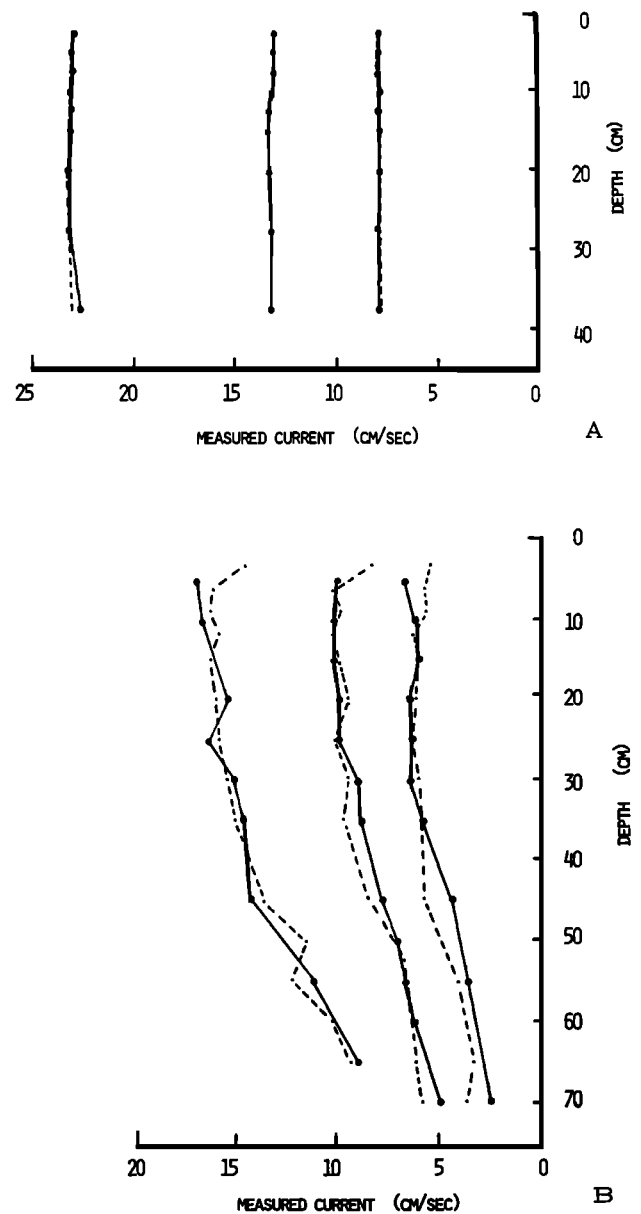


Fig. 8. Comparison of the current profiles with (dashed lines) and without (solid lines) waves: at (a) station 5 (waves propagating against the current) and (b) station 8 (waves propagating with the current).

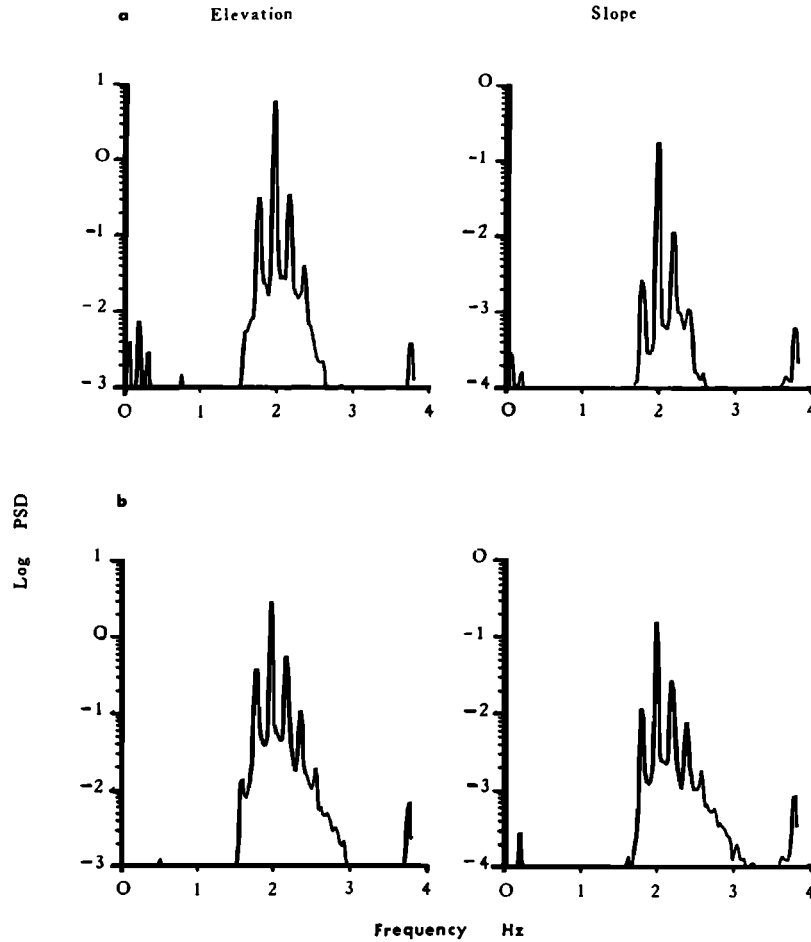


Fig. 9. Frequency spectra showing the kinematic conservation of the waves for the case of waves propagating against the current varying from 5.31 cm/s to 8.08 cm/s at stations 8 and 5. Though the wave number change is clearly visible, there is no change in the apparent frequency. (a) Elevation and slope spectra at station 8, $u = 5.31$ cm/s. (b) Elevation and slope spectra at station 5, $u = 8.08$ cm/s.

which the slope of the surface can be computed. The slope data s_r are defined here as

$$s_r = (\zeta_1 - \zeta_2)/r \quad (2)$$

in which r is the spacing between the probes and ζ_1 and ζ_2 are the two elevation readings. Since differencing is a serious source of noise generation, special care has to be taken in this step to minimize the noise. Here the same method is adopted as used by *Huang et al.* [1984], who forced the two probes to have the same rms wave elevation to eliminate any calibration error. The slope so obtained, however, is still an approximation. The spectrum of the slope can be shown to be

$$Sr(n) = k^2\Phi(n)[2(1 - \cos kr)/(kr)^2] \quad (3)$$

where $Sr(n)$ is the slope spectrum, $\Phi(n)$ is the elevation spectrum, n is the apparent frequency, and k is the wave number. For our experiments, the shortest wave lengths studied were of the order of 0.30 m, and the spacing of the probe was at a fixed 0.01 m; therefore the value of kr was at most 0.2. Then the difference between $Sr(n)$ and the true slope spectrum is an approximate factor of

$$2[1 - (kr)^2/(2 \cdot 3!)]$$

which is less than four parts per thousand from unity, an error well within the present experimental accuracy. Thus the slope spectrum obtained here is treated as the true slope spectrum and is hereinafter written without the subscript r , i.e.,

$$Sr(n) = S(n) = k^2\Phi(n) \quad (4)$$

From (4), one can compute the wave number as

$$k = [S(n)/\Phi(n)]^{1/2} \quad (5)$$

Since the wave number is derived from a ratio of the slope and the energy spectra, it is independent of the calibration of the wave probes. Because the wave number is also a function of the apparent frequency n , one can carry the computation one step further to obtain the apparent phase velocity C , as

$$C = n/k = n/[\Phi(n)/S(n)]^{1/2} \quad (6)$$

The apparent frequency and the apparent phase velocity all contain the influence of the current, which can be shown as follows. According to the kinematic conservation law of the waves, we have

$$\frac{\partial k}{\partial t} + \nabla n = 0 \quad (7)$$

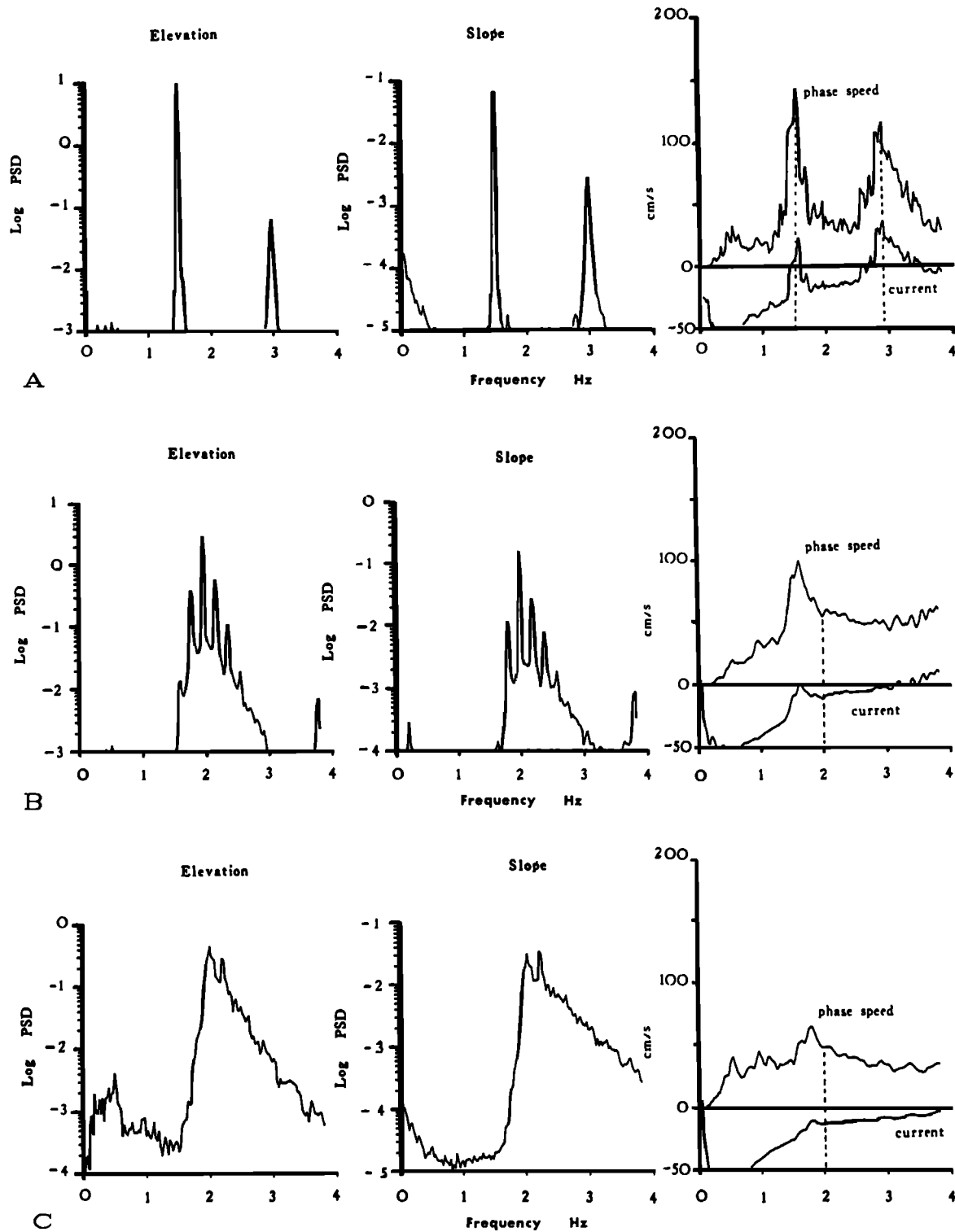


Fig. 10. Sample results of the phase and current velocities inferred from the wave elevation-slope spectra. (a) Waves consisting of a monochromatic train with harmonic components propagating with the current. Notice that the harmonics and the primary peaks all propagate at the same phase velocity. (b) Waves consisting of the primary train with various side bands propagating against the current. (c) Waves consisting of a broad band ensemble of components propagating against the current.

Under the steady state condition, (7) reduces to

$$\nabla n = 0$$

which implies

$$n = \sigma + ku = \text{const}$$

where σ is the intrinsic frequency. Typical data from the experiments presented in Figures 9a and 9b show that the apparent frequency is indeed an invariant for the rather short waves of 2.0 Hz (wavelength without current equals 0.40 m) propagating over a current varying from 0.05 to 0.08 m/s.

(8)

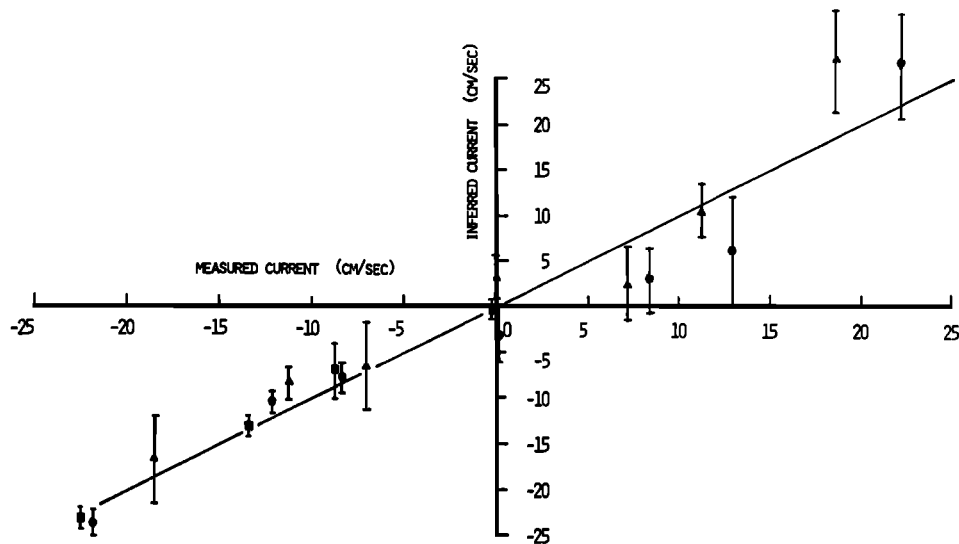


Fig. 11. Comparison between the inferred current from the elevation-slope spectra and the measured current by the EM current meter at station 3 (triangles), station 4 (circles), and station 5 (squares).

The two spectra in Figure 9a show the wave with a peak at 2.0 Hz and side bands approaching the false bottom sections. Even at the station over the flat top of the false bottom where the current has its highest value, the peak is still at 2.0 Hz. Visual observation, however, indicate a clear change of wave lengths, which is confirmed by the wave number data to be discussed later.

Since the dispersion relationship applies only to the intrinsic frequency, it follows that by dividing k through (8),

$$C = c + u \quad (9)$$

with c indicating the intrinsic phase velocity. Sample results

from the experiments are presented in Figures 10a, 10b, and 10c, representing typical monochromatic waves, monochromatic waves with side bands, and monochromatic waves degenerated into broad band after breaking. There are three panels in each figure: the left panel shows the energy spectrum; the center panel shows the slope spectrum, and the right panel shows the apparent phase velocity as computed according to (6), which is the sum of the ambient current and the intrinsic phase velocity. With the intrinsic phase velocity given at each frequency band, one can compute current for each frequency band from each set of elevation and slope data according to (9), as long as the

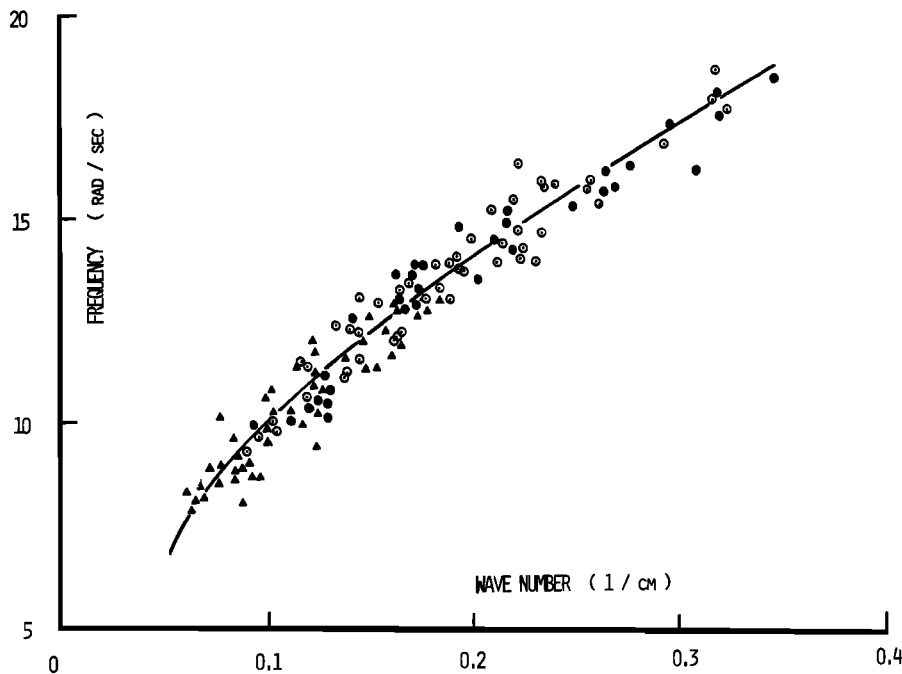


Fig. 12. The measured dispersion relationship for breaking and nonbreaking waves: nonbreaking wave with the current (solid circles), nonbreaking wave with the opposing current (solid triangles), breaking wave (circles), and the linear dispersion relationship (line).

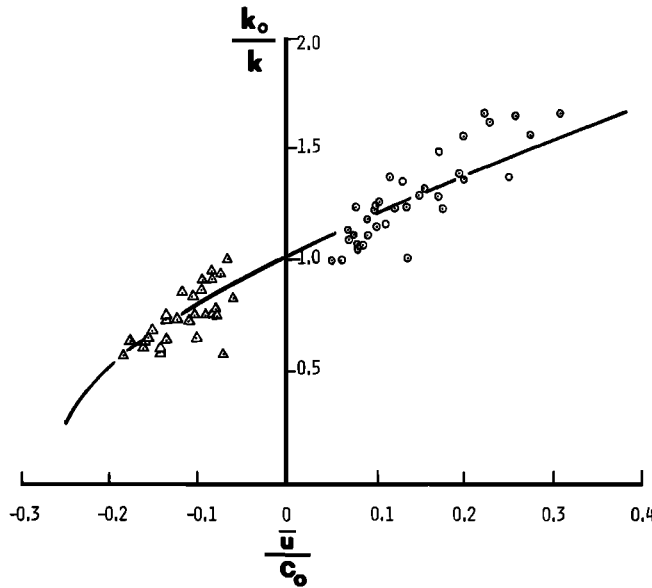


Fig. 13. Comparison between data and the theoretical result of the relation between k_0/k and u/c_0 for nonbreaking waves: circles show data for waves with the current, triangles show data for waves with the opposing current, and the line shows the theoretical result as given by equation (12).

waves are free propagating ones. To minimize the spurious error derived from a single frequency band (band width of 0.025 Hz) reading, the inferred current is based on the averaging of three spectral points which represents a band width of 0.075 Hz. These averaged current values have a typical standard deviation of 30%.

Figure 10a shows a gentle monochromatic wave train ($ak \approx 0.104$) with its harmonic propagating with the current. After the intrinsic phase velocity is deducted, both the primary and the second harmonic peaks have a positive residue similar to the directly measured values. Figure 10b shows a monochromatic wave train having a moderate steepness ($ak \approx 0.128$) with many side bands produced by Benjamin-Feir instability propagating against the current. After the intrinsic phase velocity is deducted the wave at the frequency band around 2 Hz shows a slightly negative current as directly measured. It should be pointed out that the side bands are not free waves; therefore they are nondispersive. So the residue values other than the peak reading do not represent additive current magnitudes. Figure 10c shows a rather steep wave train ($ak \approx 0.147$) propagating against the current. Owing to fast side band development and steepening by the current, the sharp-crested waves suffer some breaking at the strongest current gradient location. The combination of rich harmonics, side bands, and breaking makes the spectrum appears broad band. Even in this case, the residue again reveals a negative value as measured directly.

The values of inferred currents are grouped together to compare with depth averaged values from directly measured data. The results are presented in Figure 11 for stations 3, 4, and 5. As was shown previously, the effects of waves on currents are small, so that the measured depth-averaged currents under different wave conditions remain constant. The corresponding inferred currents do show some variation. In comparing with measured values, the inferred cur-

rents in Figure 11 represent the averaged values of four different wave conditions under the same undisturbed current. The results show a rather good agreement, especially in the wave opposing the current cases. In general, a larger standard deviation exists in the wave following the current cases.

Another way to check the kinematics of the wave-current interaction is to examine the dispersion relationship. From (8), one can rewrite the intrinsic frequency in terms of the observed quantities as:

$$n - ku = \sigma = [gk]^{1/2} \quad (10)$$

The results of this computation are presented in Figure 12 together with the theoretical dispersion relationship. The agreement between the measured wave number and the inferred intrinsic frequency using the measured current follows the linear dispersion relationship very well. It should be pointed out that the nonlinear effects in the dispersion relation is still very small in our case. For a steepness of $ak \approx 0.2$, say, the nonlinear effect can only cause a deviation of 2%. Such a deviation is too small for us to detect in this experiment.

Finally, we examine the variations of the wave number along the tank. Let the subscripts i and 0 indicate the quantities at the i th station, and zero current reference case, and then, according to Mei [1983], the kinematic conservation will give

$$\left[\frac{k_0}{k_i} \right]^{1/2} = \frac{C_i}{C_0} = \frac{1}{2T} \left[1 + \left(1 + 4T \frac{u_i}{C_0} \right)^{1/2} \right] \quad (11)$$

in which T is

$$T = \left[1 + \frac{u_0}{C_0} \right] \frac{\tanh k_0 h_0}{\tanh k_i h_i}$$

with h as the water depth.

For our cases, the waves were all in deep water, so (11) is reduced to

$$\left[\frac{k_0}{k_i} \right]^{1/2} = \frac{C_i}{C_0} = \frac{1}{2} \left[1 + \left(1 + 4 \frac{u_i}{C_0} \right)^{1/2} \right] \quad (12)$$

The value of k_0/k_i was plotted against u_i/C_0 in Figure 13 together with the theoretical curve. All the data points can be seen to fall tightly along the theoretical curve.

3.3. Breaking Waves

For opposing currents, wave breaking and blockage have been observed in several cases which will be discussed in this section. The waves, breaking or nonbreaking, are measured the same way. There are two types of breaking, a relatively gentle one and a much more violent one. Both are accompanied by a sudden downshift of the frequency at the energy spectrum peak. The kinematics of both types of breaking is illustrated by specific examples as follows.

Let us discuss the gentle breaking first. For run 69, a 2.0-Hz wave train was generated against a depth-averaged current of 8.02 cm/s. Along the path of the waves, the spectra are shown in Figures 14a–14f, which represent spectra at stations 8, 6, 5, 4, 3, and 1 with the spectrum at station 8 superimposed on each spectrum in dotted lines as a

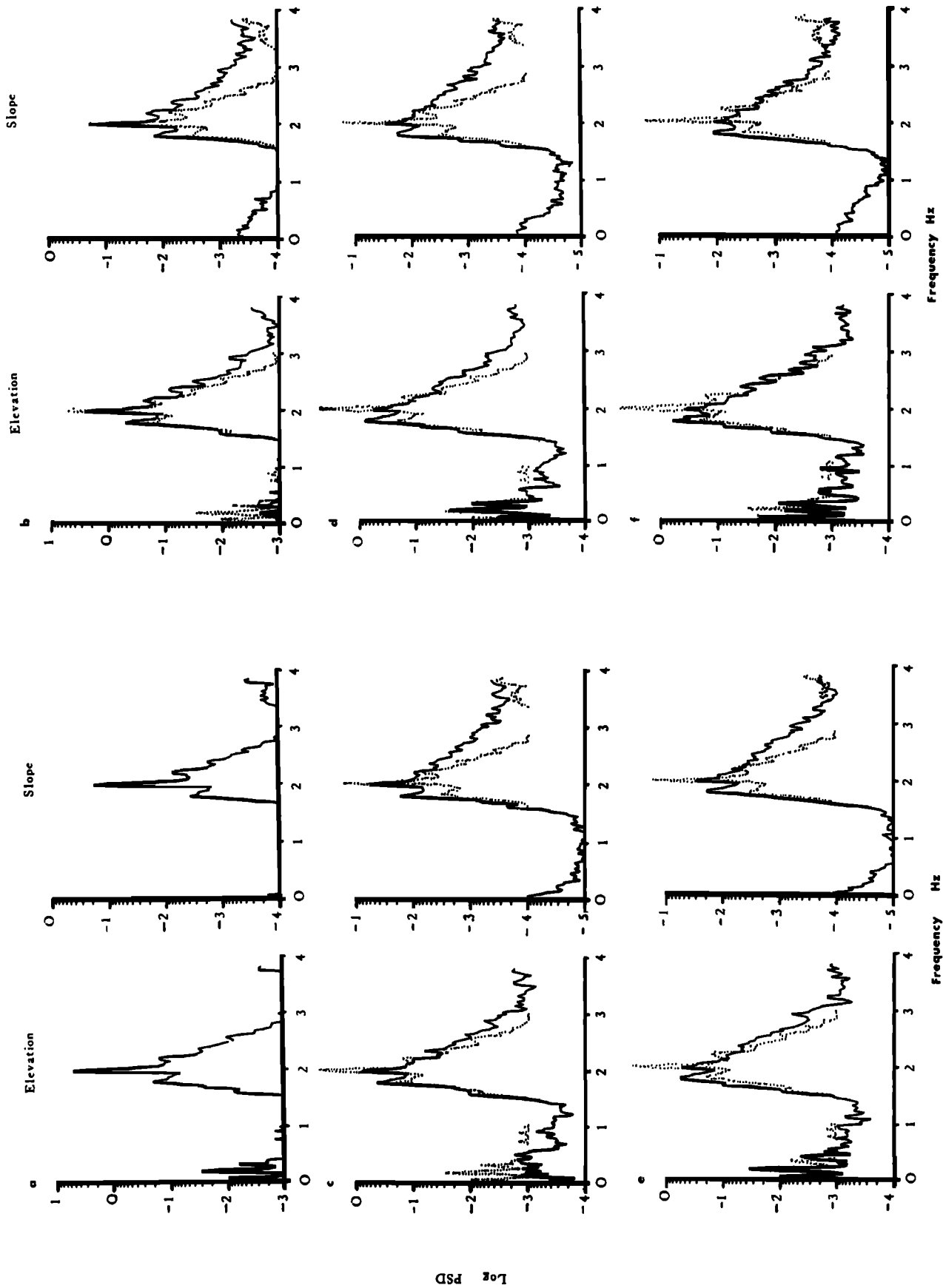


Fig. 14. Typical sequence of spectral variations for the gentle breaking waves propagating against the current, with the spectra representing stations (a) 8, (b) 6, (c) 5, (d) 4, (e) 3, and (f) 1. The dotted lines are the spectra at station 8 superimposed as a reference.

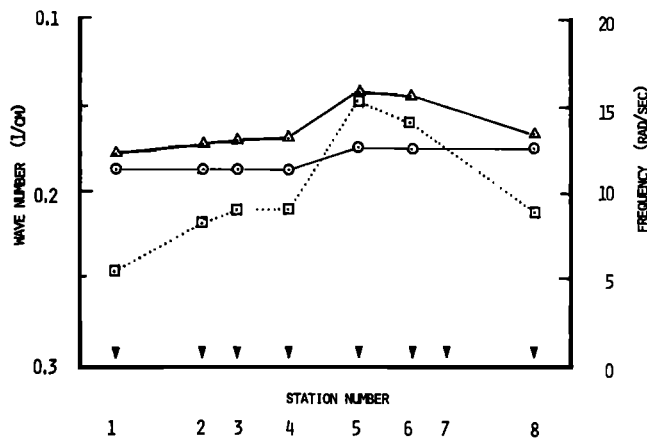


Fig. 15. Variation of the apparent frequency (circles), intrinsic frequency (triangles), and the wave number (squares) for the gentle breaking shown in Figure 14.

reference. Starting from station 8, as shown in Figure 14a, one can clearly identify the peak of the spectrum at 2.0 Hz and numerous side bands from the spectrum. As the waves propagated, the side bands grow relative to the peak. Between stations 5 and 4, breaking at a sharply formed crest is observed visually. Correspondingly, the peak of the spectrum shifts down to a lower frequency value. This energy shift is a continuous process. By station 1 the frequency of the dominant peak is clearly below 2.0 Hz. Even though there is a wave breaking event, the total energy as indicated by the spectra does not seem to have decreased substantially. This type of breaking is most likely caused by the frequency down shift. It is a typical case of the normal mode instabilities as discussed by *Longuet-Higgins and Cokelet* [1978], which does not require the direct influence of the currents. The current, however, can have an indirect effect by shortening the wave length and increasing the steepness of the waves (as shown in Figure 15), which can hasten the growth of the side band and therefore enhance the instabilities as predicted by the nonlinear theory [Phillips, 1977]. Here, before the breaking, the apparent frequency is constant, but the intrinsic frequency and wave number increase steadily. After the wave breaks, the apparent frequency shifts, and thereafter maintains a constant lower value. The intrinsic frequency and the wave number, however, decrease drastically.

The second type of breaking is a much more energetic event. In run 75, a train of 2.0-Hz waves is propagating against a depth-averaged current of 13.3 cm/s at station 8. By the time the waves reach the test section, the frequency of the spectral peak has already downshifted to around 1.5 Hz. The spectra show a rather broad band characteristic as can be seen in Figures 16a–16f, which represent the spectra at the stations similar to those in run 69. The breaking occurs much sooner at station 6 where the local current value has reached 19.6 cm/s which is the theoretical blockage for the 1.5-Hz wave. The breaking here is quite violent, as is reflected by the drastic energy decrease after the breaking. The turbulence generated by the currents and the breaking waves is strong enough to suppress all the small waves and make the surface quite smooth as is shown by the slope spectra. Although the peak frequency stays around a similar value, the shape of the spectra change drastically, and the

levels of the peaks drop 1 order of magnitude; waves having frequencies greater than 2.0 Hz practically disappear altogether.

Summaries of the kinematic characteristics of the breaking wave cases are given in Figures 12 and 17. In Figure 12, the breaking wave cases are represented by the solid circles. They follow the dispersion relationship very well. In Figure 17, the ratio of the wave number is shown as a function of \bar{u}/C_0 . In general, most of the data still follow the theoretical result as indicated by the solid line computed from equation (11) except during breaking. Of special interest here are the variations of k_0/k as a function of \bar{u}/C_0 for the two blocking cases from station to station. For run 75, the sequence of events is indicated by the dotted line. The wave number maintains constant at the beginning, with \bar{u}/C_0 at -0.18 and k_0/k around 0.8, then both \bar{u}/C_0 and k_0/k values decrease to the lowest value at station 5, where the current reaches its highest values, and the \bar{u}/C_0 value is near the $-1/4$ limit as predicted theoretically. After station 4 the waves disintegrate completely, and no more meaningful wave data can be extracted.

A similar trend occurs in run number 77. Here the velocity is just below the theoretical blocking limit; therefore the wave condition can be traced for all the stations as indicated in Figure 17. The starting point of this case is also at station 8, where the \bar{u}/C_0 value is around -0.14 and k_0/k is 0.75. As the waves propagate further into the opposing current, the wave number increases drastically after a slight initial decrease. At station 5, where the current reaches its maximum value, the \bar{u}/C_0 value approaches -0.23 . Then the wave number decreases as the velocity decreases. Finally, at station 1, the condition returns almost to that of station 8; the \bar{u}/C_0 and the k_0/k values also return to the initial values.

In no case in our experiment did the \bar{u}/C_0 value reach beyond the theoretical limit of $-1/4$. Thus the theoretical blockage limit of $\bar{u}/C_0 = -1/4$ is also confirmed.

4. DISCUSSIONS AND CONCLUSIONS

In this paper, only the kinematics of the strong wave-current interactions has been discussed. In order to discuss the dynamics, the absolute accuracy of the wave probes and detailed monitoring of the turbulence properties in the currents are required. Although the wave probes used have been shown to have an accuracy of 5% [Huang and Long, 1980], the wave amplitudes measured from station to station under variable currents sometimes suffered more than a 50% fluctuation between stations. After repeated checks of the probes and the measurement and data analysis procedures, no error can be identified. These large fluctuations observed could be the result of breaking waves as discussed by *Thomas* [1981]. To overcome these difficulties, one would have to monitor the turbulence conditions at the station of wave breaking in detail to repeat the wave measurements eight times (once with each probe pair measuring each station) and seek the overall mean in each case in order to eliminate any possible error in absolute calibration. Such a test is not possible to schedule at present. Since the kinematics depends only on the ratio of the measurements, we decided to report the results on this aspect first.

Even in limiting our consideration to just the kinematics, the scarcity of experimental data compared with the theoretical results is alarming. The urgent need for such data was

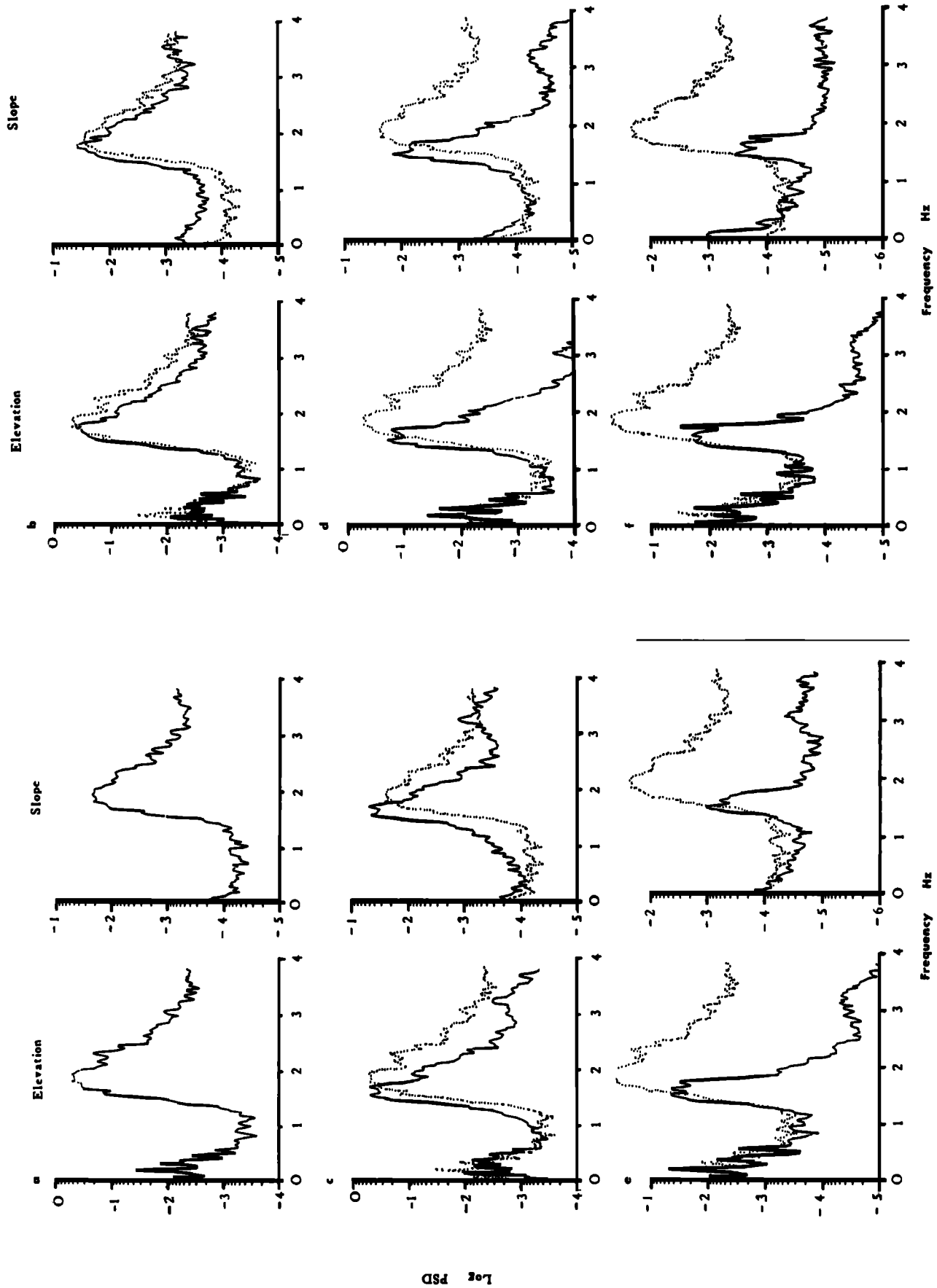


Fig. 16. Typical sequence of spectral variations for the violent breaking waves caused by blocking, with the spectra at station 8 superimposed as a reference and with the same sequence in Figure 14. Breaking starts at station 5, and continues to station 4.

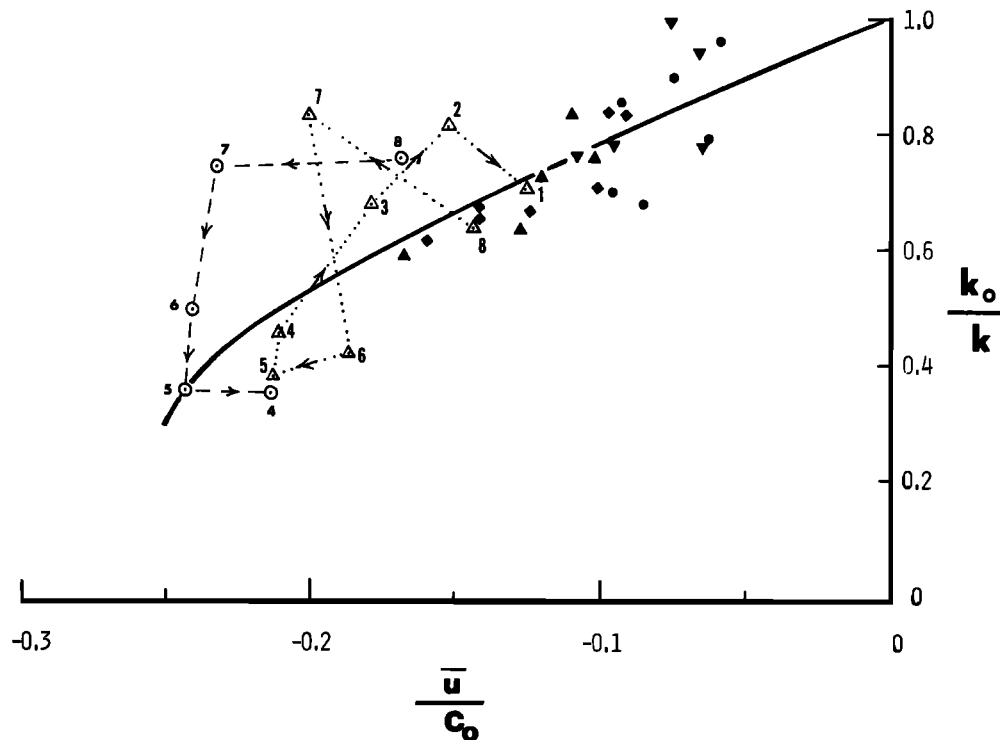


Fig. 17. Relationship between k_0/k and u/c_0 for breaking wave cases. Run 75 (dashed lines with open circles) and run 77 (dotted lines with open triangles) are blocking cases. The station numbers are indicated by numbers beside the symbols. The arrows in each case trace the developments from station 8 to the last station where waves still can be identified. All other solid symbols are for gentle breaking cases.

clearly stressed by *Peregrine* [1976], but difficulties encountered in the measurements have severely limited the number of investigations. The earlier experimental studies of current-wave interaction conducted by *Yu* [1952], and *Evans* [1955] were all concentrated on the wave breaking caused by opposing currents. *Yu's* results suffered two deficiencies: first, the current was not measured directly, but inferred by volume of discharge; second, he used a wrong energy equation to compute the wave height, thus casting some doubt on the comparison between the theoretical and the experimental results. Interestingly, he did find the blockage limit at \bar{u}/C_0 equal to $-1/4$, which is in agreement with the findings of the present results. *Evans* [1955] also conducted experiments on the breaking limit with currents confined only to the surface layer. He found the same blockage as reported here.

Later, *Plate and Trawle* [1970] and *Long and Huang* [1976] conducted experiments with wind-generated waves in the presence of water currents. The study of *Long and Huang* [1976] was more oriented toward the dynamics. They studied the variation of the wind wave spectra over spatially nonuniform currents. Although the spectra showed the Doppler shifts clearly, no quantitative kinematic information was derived. The study of *Plate and Trawle* [1970] was conducted on spatially uniform currents. They found the phase velocity of the waves following the classical dispersion relationship with a simple Doppler shift.

Subsequent studies by *van Hoften and Karaki* [1976] and *Brevik and Aas* [1980] were more concerned with the shallow water wave energy dissipation caused by turbulence in strong shear currents. Recently, *Thomas* [1981] conducted

both numerical and experimental studies of the wave-shear current interactions. He found that even for currents with an arbitrary distribution of vorticity, the variations of wave length and amplitude can be accurately predicted simply on the basis of the irrotational wave-current interaction model with a depth averaged mean current. This conclusion is confirmed by the present experiments. It also gives us the justification in processing the current data as a depth-averaged mean, even though there are some slight vertical shears.

None of the previous studies have included a current with a spatial gradient, and none of them have documented the kinematics in all the aspects. In the present study, a current with a spatial gradient was used, and the kinematics was extensively tested against the existing theory. Based on these experiments, the following conclusions can be drawn. (1) The kinematic conservation of the waves as given in equation (7) was confirmed for the steady state condition. (2) The variations of the phase velocity, the wave length, the intrinsic frequency, and the blockage limit for waves propagating against currents agree well with the values predicted by the formulae derived from the kinematic conservation and the dispersion relation.

Acknowledgments. This work is supported in part (R.J.L. and N.E.H.) by a contract from the Office of Naval Research Fluid Dynamics Program and Naval Laboratory Participation Program (NLPP), and in part (S.R.L.) by the NASA Supporting Research and Technology Program from the Oceanic Processes Branch. The authors also wish to thank Larry Bliven for his assistance in the laboratory phase of the experiment and in the computations. The

experiments were conducted while N.E.H. was on a detail duty to the ONR Physical Oceanography Program.

REFERENCES

- Aubrey, D. G., and J. H. Trowbridge, Kinematic and dynamic estimates from electromagnetic current meter data, *J. Geophys. Res.*, **90**, 9137-9146, 1985.
- Bliven, L. F., N. E. Huang, and S. R. Long, Experimental study of the influence of wind on Benjamin-Feir sideband instability, *J. Fluid Mech.*, **162**, 237-260, 1986.
- Brevik, I., and B. Aas, Flume experiment on waves and currents, I, Rippled bed, *Coastal Eng.*, **3**, 149-177, 1980.
- Evans, J. T., Pneumatic and similar breakwaters, *Proc. R. Soc. London, Ser. A*, **231**, 457-466, 1955.
- Gerber, M., The Benjamin-Feir instability of a deep-water Stokes wavepacket in the presence of a non-uniform medium, *J. Fluid Mech.*, **176**, 311-332, 1987.
- Gonzalez, F. I., A case study of wave-current-bathymetry interactions at the Columbia River entrance, *J. Phys. Oceanogr.*, **14**, 1065-1078, 1984.
- Guza, R. T., Comment on "Kinematic and dynamic estimates from electromagnetic current meter data" by D. G. Aubrey and J. H. Trowbridge, *J. Geophys. Res.*, **93**, 1337-1343, 1988.
- Huang, N. E. and S. R. Long, An experimental study of the surface elevation probability distribution and statistics of wind generated waves, *J. Fluid Mech.*, **101**, 179-200, 1980.
- Huang, N. E., S. R. Long, C. C. Tung, and L. F. Bliven, The non-Gaussian joint probability density function of slope and elevation for a nonlinear gravity field, *J. Geophys. Res.*, **89**, 1961-1972, 1984.
- Long, S. R., and N. E. Huang, Observations of wind-generated waves on variable current, *J. Phys. Oceanogr.*, **6**, 962-968, 1976.
- Longuet-Higgins, M. S., A stochastic model of sea-surface roughness, I, Wave crests, *Proc. R. Soc. London, Ser. A*, **410**, 19-34, 1987.
- Longuet-Higgins, M. S., and E. D. Cokelet, The deformation of steep surface waves on water, II, Growth of normal mode instabilities, *Proc. R. Soc. London, Ser. A*, **360**, 489-505, 1978.
- Mallory, J. K., Abnormal waves on the southeast coast of South Africa, *Int. Hydro. Res.*, **51**, 99-129, 1974.
- McClain, C. R., N. E. Huang, and P. E. LaViolette, Measurements of sea state variations across oceanic fronts from laser profilometry, *J. Phys. Oceanogr.*, **12**, 1228-1244, 1982.
- Mapp, G. R., C. S. Welch, and J. C. Munday, Wave refraction by warm core rings, *J. Geophys. Res.*, **90**, 7153-7162, 1985.
- Mei, C. C., *The Applied Dynamics of Ocean Surface Waves*, Wiley-Interscience, New York, 1983.
- Mollo-Christensen, E., Surface wave modulation pattern in radar images, *Nav. Res. Rev.*, **34**, 41-50, 1982.
- Peregrine, D. H., Interaction of water waves and currents, *Adv. Appl. Mech.*, **16**, 9-117, 1976.
- Peregrine, D. H. and I. G. Jonsson, Interaction of waves and currents, *CERC MR 83-6*, 88 pp., U.S. Army Corps of Engineers, Vicksburg, Miss., 1983.
- Phillips, O. M., *The Dynamics of the Upper Ocean*, 2nd Ed., Cambridge University Press, New York, 1977.
- Plate, E., and M. Trawle, A note of the celerity of wind waves on a water current, *J. Geophys. Res.*, **75**, 3537-3544, 1970.
- Thomas, G. P., Wave-current interactions: An experimental and numerical study, I, Linear waves, *J. Fluid Mech.*, **110**, 457-474, 1981.
- van Hoften, J. D. A., and S. Karaki, Interaction of waves and turbulent current, in *Proceedings of the 15th Coastal Engineering Conference*, vol. 1, pp. 404-422, American Society of Civil Engineers, New York, 1976.
- Yu, Y. Y., Breaking of waves by an opposing current, *Eos Trans. AGU*, **33**, 39-41, 1952.
- Yuen, H. C., and B. M. Lake, Nonlinear dynamics of deepwater gravity waves, *Adv. Appl. Mech.*, **22**, 69-229, 1982.

N. E. Huang, Office of Naval Research, Arlington, VA 22217.
R. J. Lai, Code 1561, David Taylor Research Center, Bethesda, MD 20084.

S. R. Long, NASA Goddard Space Flight Center, Wallops Flight Facility, Wallops Island, VA 23337.

(Received June 27, 1988;
accepted January 16, 1989.)